J. Mech. Phys. Solids 181 (2023) 105452

Contents lists available at ScienceDirect

Journal of the Mechanics and Physics of Solids

journal homepage: www.elsevier.com/locate/jmps

Stabilization against gravity and self-tuning of an elastic variable-length rod through an oscillating sliding sleeve

P. Koutsogiannakis, D. Misseroni, D. Bigoni, F. Dal Corso *

DICAM, University of Trento, via Mesiano 77, I-38123 Trento, Italy

ARTICLE INFO

Keywords:
Elastica
Configurational mechanics
Dynamic bifurcation

ABSTRACT

An elastic rod, straight in its undeformed state, has a mass attached at one end and a variable length, due to a constraint at the other end by a frictionless sliding sleeve. The constraint is arranged with the sliding direction parallel to a gravity field, in a way that the rod can freely slip inside of the sleeve, when the latter is not moving. In this case, the free fall of the mass continues until the rod is completely injected into the constraint. However, when the sliding sleeve is subject to a harmonic transverse vibration, it is shown that the fall of the mass and the rod injection are hindered by the presence of a configurational force developing at the sliding sleeve and acting oppositely to gravity. During the dynamic motion, such a configurational force is varying in time because it is associated with the variable bending moment at the sleeve entrance. It is (experimentally, analytically, and numerically) demonstrated that, in addition to the states of complete injection or ejection of the elastic rod (for which the mass falls down or is thrown out), a stable sustained oscillation around a finite height can be realized. This 'suspended motion' is the signature of a new attractor, that arises by the constraint oscillation. This behaviour shares similarities with parametric oscillators, as for instance the Kapitza inverted pendulum. However, differently from the classical parametric oscillators, the 'suspended' configuration of the rod violates equilibrium and the stabilization occurs through a transverse mechanical input, instead of a longitudinal one. By varying the sliding sleeve oscillation amplitude and frequency within specific sets of values, the system spontaneously adjusts the sustained motion through a self-tuning of the rod's external length. This self-tuning property opens the way to the design of vibration-based devices with extended frequency range.

1. Introduction

The Kapitza inverted pendulum is a famous example of a parametric oscillator showing that an unstable equilibrium configuration for a rigid and movable structure can be dynamically stabilized through a controlled time-harmonic vibration, acting at the basis of the pendulum and aligned parallel to the gravity (Kapitza, 1951). The aim of the present article is to disclose how a similar, but more complex, phenomenon can be displayed by a variable length elastic structure through a controlled time-harmonic vibration orthogonal to the gravity direction. In particular, an *elastic flexible rod* is arranged in a sort of inverse pendulum configuration (Fig. 1, left), where the lower part is constrained by a (frictionless) sliding sleeve and the other end has a lumped mass attached. In the presence of a gravitational field and in the absence of any disturbance, including any motion of the constraint, the free fall motion would occur for the mass through the injection into the sliding sleeve of the rod, remaining undeformed. Therefore, contrary to the Kapitza pendulum, *the straight upward configuration never represents an equilibrium configuration*. Despite this difference, it is

* Corresponding author.
E-mail address: francesco.dalcorso@unitn.it (F. Dal Corso).

https://doi.org/10.1016/j.jmps.2023.105452
Received 6 April 2023; Received in revised form 30 June 2023; Accepted 28 September 2023
Available online 6 October 2023

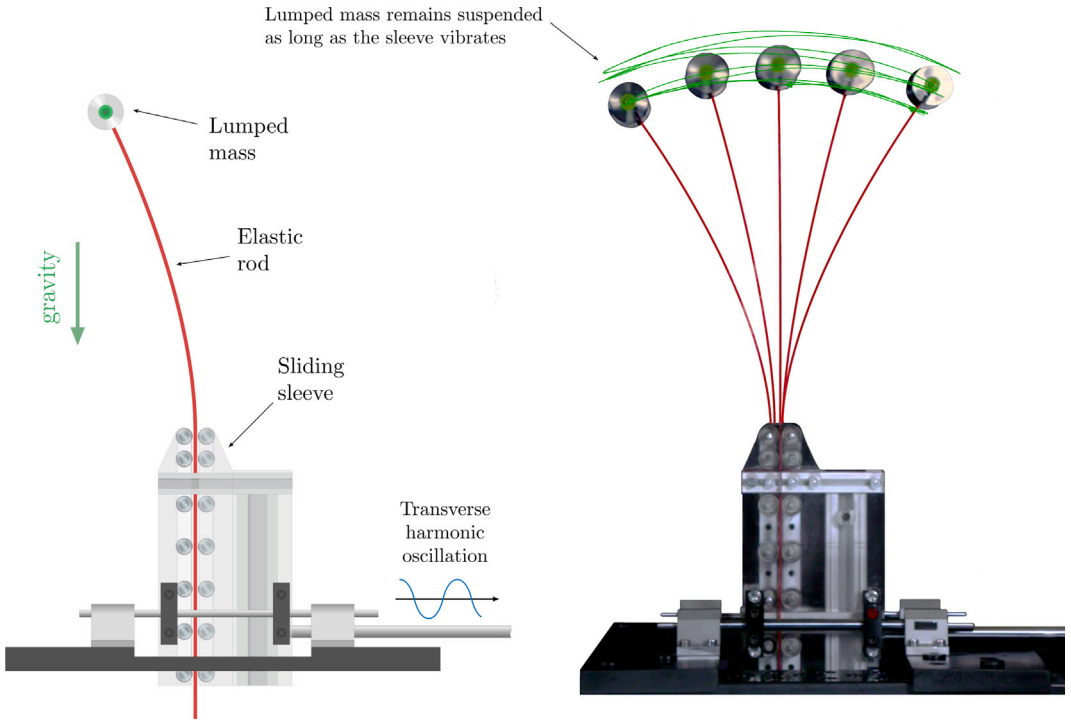

Fig. 1. (Left) Concept drawing of the experimental setup, where an elastic rod with a lumped mass attached at its top end is inserted inside a sliding sleeve, with direction parallel to the gravity. While the mass would simply fall down when the constraint does not move, the mass may oscillate suspended against gravity when the constraint is sinusoidally vibrating along the horizontal direction. (Right) The suspended motion is shown through a superimposed photo sequence and the tracked trajectory of the mass centre (green line).

shown that a transverse time-harmonic oscillation of the sliding sleeve may generate a stable periodic or quasi-periodic motion around a finite value of the external length of the rod. In practice, this is displayed as a 'mass swinging suspended in the air', as experimentally demonstrated through the photo sequence reported in Fig. 1 (right). Noteworthy, the imposed constraint vibration is *transverse* to the gravity direction, marking another difference with respect to the Kapitza pendulum, where the vibration is instead parallel.

The sustained motion shown in Fig. 1 (right), which is theoretically, numerically, and experimentally demonstrated in the following sections, is made possible by the elastic flexibility of the rod, so that it would be impossible to be observed in a rigid system such as the Kapitza pendulum. More specifically, when constraining a flexurally deformed rod, the sliding sleeve generates a configurational force contrasting gravity and proportional to the square of the bending moment at the sliding sleeve entrance. This configurational force was recently shown to act on elastic rods with variable length subject to bending (Bigoni et al., 2015; Hanna et al., 2018; O'Reilly, 2017, 2015; Wang and Detournay, 2022), torsion (Bigoni et al., 2014), and analysed for buckling (Liakou, 2018a,b). As a result, the configurational force represents the structural counterpart of the driving force on defects, as conceptualized in Eshelbian mechanics (Eshelby, 1999); see also a recently provided mechanical interpretation (Ballarini and Royer-Carfagni, 2016).

The dynamics of the considered structure is characterized by two stable attractors inherent to the presence of the sliding sleeve constraint and corresponding to two possible final stages for the system, respectively associated with a vanishing and an infinite value of the external length of the rod (Armanini et al., 2019). Indeed, the rod slips inside the sleeve when the configurational force is too low, while it is ejected when the force is too high. In addition to these two inherent limit attractors, it is found that a third one may arise when a harmonic transverse oscillation of the sleeve is imposed. This third attractor is associated with a finite value for the external length of the rod, so that the mass does not simply fall down, rather, it remains suspended around a certain height. The height value depends on (i.) the amplitude and frequency of the imposed harmonic motion, (ii.) the bending stiffness of the rod, and (iii.) the (lumped) mass value. Roughly speaking, the height value is approximately given by the external length of the clamped rod which would be at resonance under the same frequency of the harmonic motion imposed to the sliding sleeve.

Finally, the oscillating sliding sleeve system is shown to display *self-tuning properties*, consisting in the spontaneous adjustment of the external length when the amplitude and frequency oscillation parameters are 'relatively slowly varying' as long as the third attractor is stable.

Attraction to a suspended non-equilibrium configuration has never been so far observed and is proven in this article through asymptotic solutions, numerical simulations, and the design, realization, and validation (at the *Instabilities Lab* of the University of Trento) of a new experimental setup permitting control and measure of the nonlinear dynamics of an elastic rod, subject to large rotations and, simultaneously, to configurational changes of very large amounts.

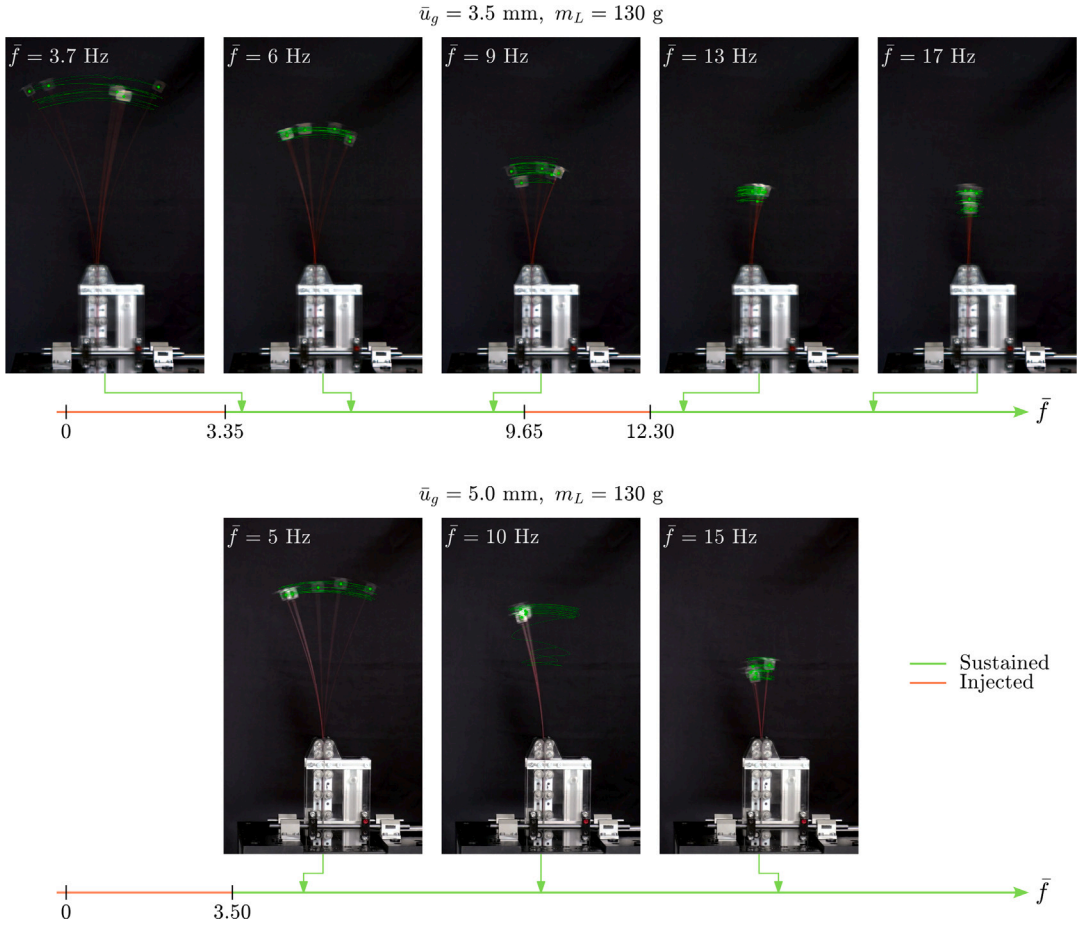

Fig. 2. A transverse vibration $u_g(t) = \bar{u}_g \cos\left(2\pi \bar{f}\, t\right)$ generates a suspended (against gravity) dynamic motion for a lumped mass $m_L = 130$ g (tracked with green line) attached at the end of an elastic rod. Photos taken at different instants of time are superimposed for specific values of frequency $\bar{f}$, showing experimental results for two different oscillation amplitudes, $\bar{u}_g = 3.5$ mm (top) and 5 mm (bottom). The green part of the $\bar{f}$ axis is associated with sustained oscillation, while the red one with final injection.

The presented results introduce a new paradigm in nonlinear structural dynamics and may find applications for positioning tasks in soft robotics (Alfalahi et al., 2020; Renda et al., 2021; Sipos and Várkonyi, 2020), as well as for wave mitigation devices (Lee et al., 2018; Liu et al., 2015; Matlack et al., 2016; Wang and Bertoldi, 2012) and environmental energy harvesters (Gibus et al., 2022; Ma et al., 2020; Yu et al., 2020), where self-tuning property can be exploited to improve efficiency and to extend the frequency range of application.

The article is organized as follows: after the experimental evidence presented in Section 2, a nonlinear elastic model of the system is developed in Section 3, together with an asymptotic solution. Numerical results from the integration of the nonlinear dynamics are provided in Section 4, showing the transition from periodic to quasi-periodic motion. Finally, the presented results are validated in Section 5 through a comparison between theoretical predictions and experimental measurements.

2. Experimental evidence of sustained motion and self-tuning of the oscillating rod

An experimental setup has been designed, manufactured, and tested (at the 'Instabilities Lab' of the University of Trento) with the purpose of observing the dynamics of a rod inserted into a sliding sleeve, as sketched in Fig. 1 (left). A detailed presentation of the experimental setup is deferred to Section 5.

The sliding sleeve is forced to sinusoidal transverse oscillations along the horizontal direction through the applied displacement $u_g(t)$, defined by

$$u_g(t) = \bar{u}_g \cos\left(2\pi \bar{f}\, t\right), \tag{1}$$

where $\bar{u}_g$ and $\bar{f}$ are respectively the amplitude and the frequency of the sliding sleeve oscillation, while t is the physical time.

When partially inserted inside of the vibrating sliding sleeve, the rod is intuitively expected to either fall down (at small oscillation amplitude or frequency) or to be ejected outside the sleeve (at high oscillation amplitude or frequency). These two behaviours do in

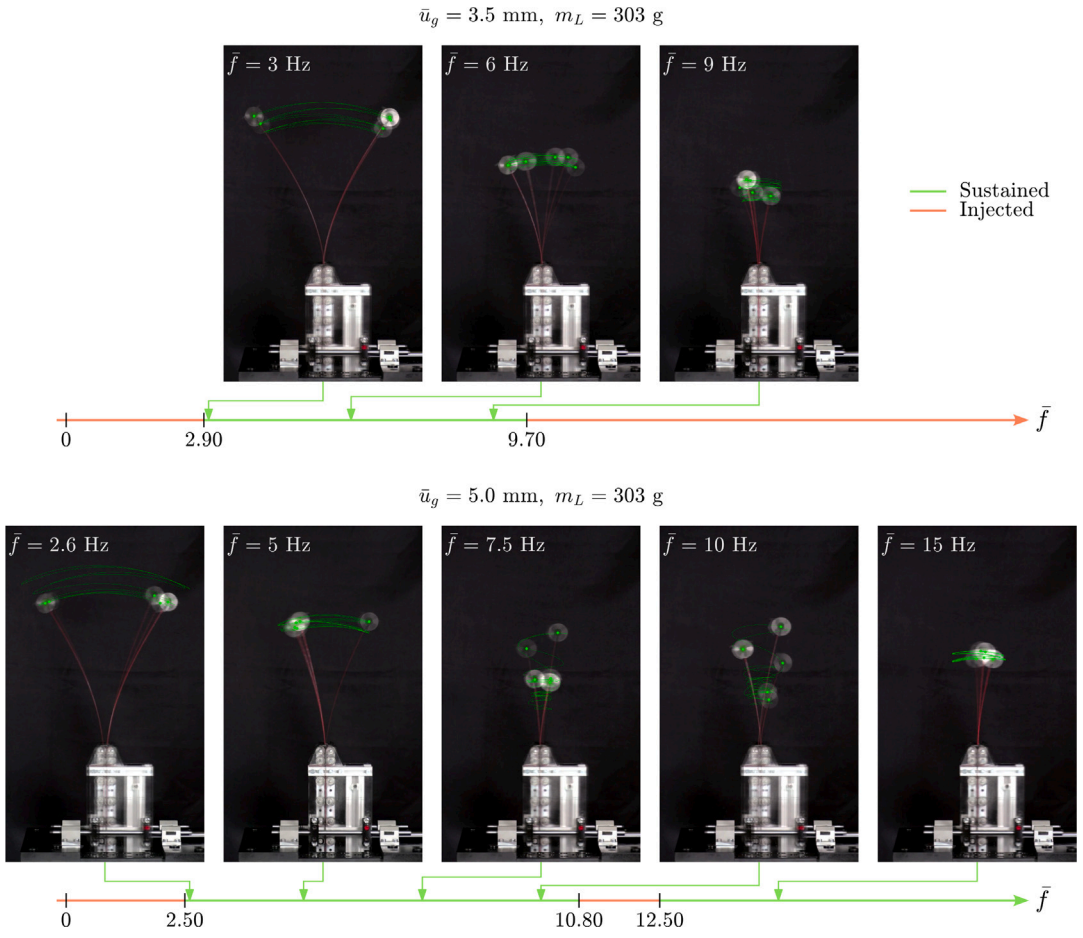

Fig. 3. As for Fig. 2, except for a lumped mass $m_L = 303$ g.

fact exist, but, interestingly, a third behaviour is found, in which the interplay of the configurational force generated at the sliding sleeve entrance with the gravity force creates a sustained motion, as shown in Fig. 1 (right) and more accurately in Figs. 2 and 3, where a series of superimposed photos, with mass tracking reported with a green line, are shown at increasing frequency $\bar{f}$ for different lumped mass m_L and oscillation amplitude $\bar{u}_g$ values. It can be appreciated that the sustained motion occurs for a height of the lumped mass varying with the frequency value, disclosing a self-tuning property of the system. Videos of the complete run of the experiments shown in Figs. 2 and 3 are available as Supplementary Material.

Since the beginning of the experimental campaign it has been observed that a sustained motion is not always displayed by the system, rather it can be achieved only within specific ranges of frequency and amplitude. With reference to the values of the lumped mass $m_L = \{130, 303\}$ g, two kinds of experiments, both starting from a situation of sustained motion (held for 1 min to overcome transient effects), have been performed:

(i) *amplitude controlled experiments* — the frequency $\bar{f}$ is held fixed at a specific constant value (ranging between 2.5 and 17 Hz) while the amplitude $\bar{u}_g$ is decreased (with a step of 0.1 mm every 10 s) until injection, which terminates the experiment at a recorded final amplitude, denoted as 'critical', $\bar{u}_{g,cr}(\bar{f})$;

(ii) *frequency controlled experiments* — the amplitude $\bar{u}_g$ is held fixed at a specific constant value ($\bar{u}_g = \{3.5, 5\}$ mm) while the frequency $\bar{f}$ is increased or decreased (with a step of 0.05 Hz every 15 s) until injection, which terminates the experiment at a recorded final frequency, denoted as 'critical', $\bar{f}_{cr}(\bar{u}_g)$.

Experiments of the type (i) lead to the results (in terms of critical amplitude $\bar{u}_{g,cr}$ versus frequency $\bar{f}$) reported in Fig. 4, where experimental measures for the above-mentioned two different values of lumped mass correspond to different markers (crosses for $m_L = 130$ g, and circles for $m_L = 303$ g). The figure shows that the sustained motion is only possible for amplitude–frequency pairs belonging to the region above the critical curve (reported as green for $m_L = 130$ g), while injection occurs when the pair belongs to the region below the critical curve (reported red for $m_L = 130$ g).

At increasing frequency, the results show an initial steep decrease of $\bar{u}_{g,cr}$, until a minimum is reached and a subsequent increase is visible, up to an isolated maximum, followed by a further mild decrease (within the measured frequency range). It follows that

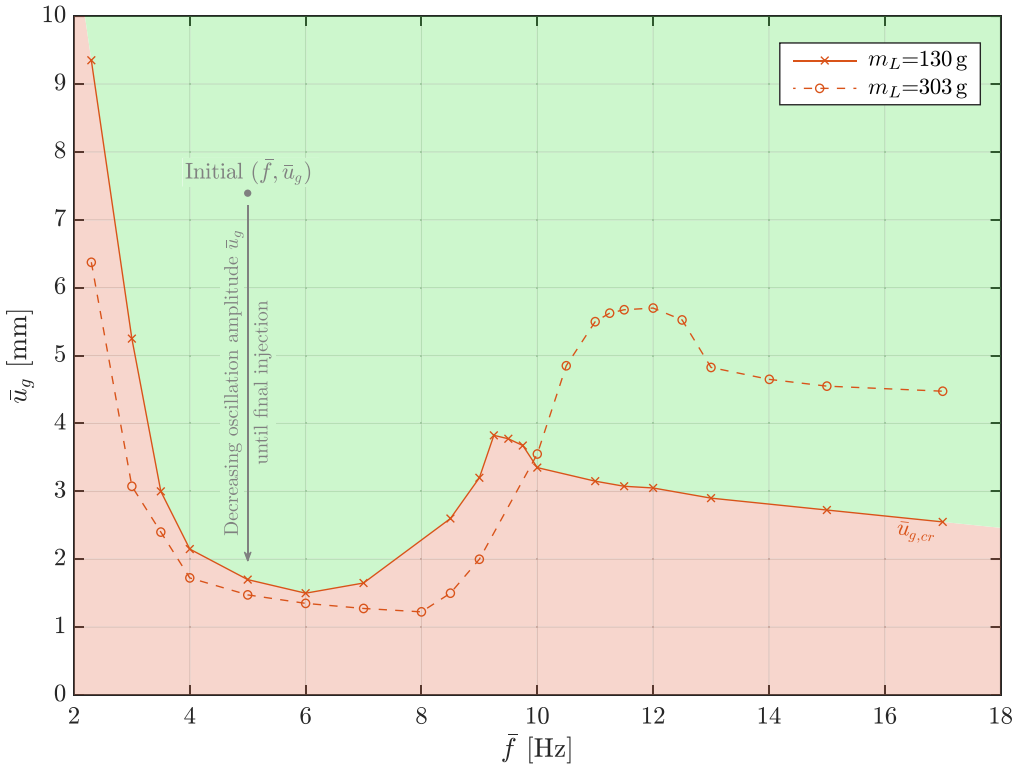

Fig. 4. Critical amplitude $\bar{u}_{g,cr}$ as a function of the frequency $\bar{f}$ (red curves). The critical curves are drawn through a linear interpolation of the critical pairs measured through type (i) experiments for $m_L = 130\,\mathrm{g}$ (red crosses) and for $m_L = 303\,\mathrm{g}$ (red circles). The critical curve defines the transition from a sustained motion (green region for $m_L = 130\,\mathrm{g}$) to the rod's final injection (red region for $m_L = 130\,\mathrm{g}$).

the sequence of tests of type (ii) experiments in order to detect the critical frequency $\bar{f}_{cr}$ may vary from at least one to at least three, due to the presence of a non-unique $\bar{f}_{cr}$ for specific ranges of $\bar{u}_g$, as visible in the videos available as Supplementary Material. In this case, the critical values have to be detected by monotonically decreasing and also monotonically increasing the frequency from different initial values. Results concerning the experiments of type (ii) are reported in Section 5, where the developed theory is tested against the experiment to further validate the critical curves reported in Fig. 4.

3. Mechanical modelling and average external length

3.1. Nonlinear equations of motion

The oscillating sliding-sleeve structure is modelled as an inextensible rod of length L, straight in its undeformed configuration, with flexural stiffness B, and partially inserted into a sliding sleeve, Fig. 5. By introducing the curvilinear coordinate $s \in [0, L]$, corresponding to the arc-length of the rod's centre line, the portion of rod constrained by the sliding sleeve is defined by the set $s \in [0, L - \ell(t)]$, while the portion external to the sliding sleeve, which is the only part that can be bent, by $s \in [L - \ell(t), L]$, being $\ell(t)$ the length of the rod external to the constraint. Note that the length L of the rod is assumed to be finite, while the case of infinite length would deserve a different treatment. A mass m is modelled as attached at the tip of the rod ($s = L$) and the sleeve is oriented in a vertical direction against gravity, defined by the acceleration g. The attached mass value m of the theoretical model is considered to be possibly different from the 'real' lumped mass value m_L in order to account for inertial effects of the rod (having a linear mass density γ), so that $m = m_L + \Delta m$, with $\Delta m \geq 0$. It is instrumental to consider two parallel Cartesian reference systems, the absolute system $X - Y$, with origin fixed at the mean position of the sliding sleeve entrance, and the relative system $x - y$, with origin attached at the moving sliding sleeve entrance and moving with it, which is forced to harmonically oscillate through the imposed displacement $u_g(t)$ (parallel to X), so that the absolute and the relative positions are related as

$$X(s,t) = x(s,t) + u_g(t), \qquad Y(s,t) = y(s,t). \tag{2}$$

Because of the rod inextensibility, in addition to the configurational parameter $\ell(t)$, the deformed configuration is described through the rotation field $\theta(s,t)$ measuring the counter-clockwise rotation of the rod's tangent with respect to the undeformed state. While the rotation is constrained to remain null within the portion of the rod inside the sliding sleeve, $\theta(s,t) = 0$ for $s \in [0, L - \ell(t)]$, the

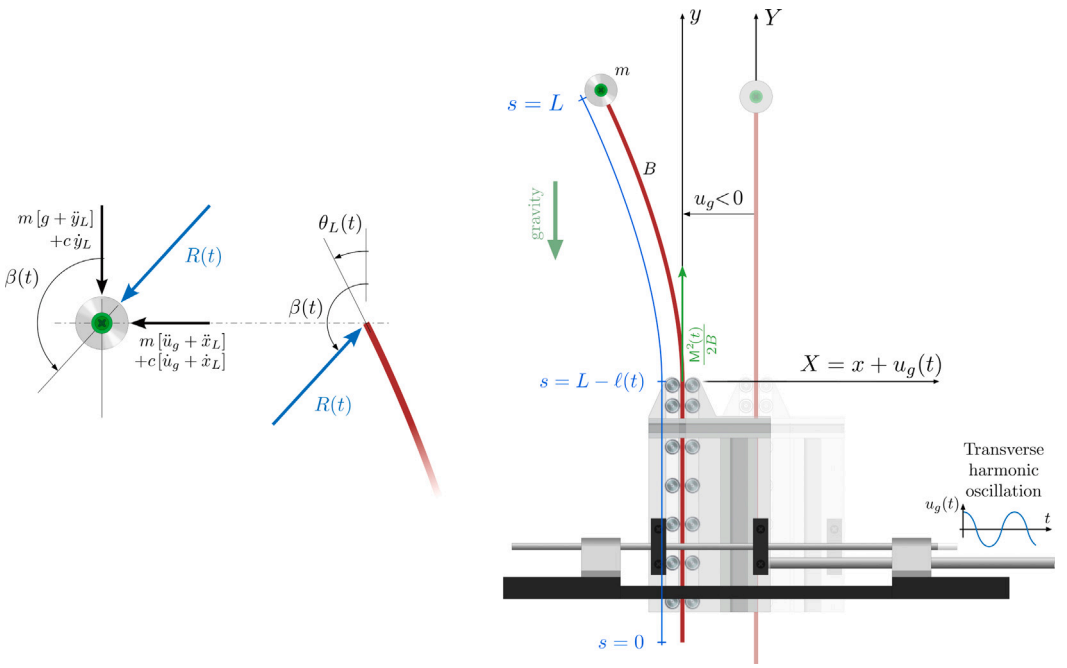

Fig. 5. An elastic rod, of flexural stiffness B and total length L, is partially inserted into the sliding sleeve so that the time-varying external length is $\ell(t) < L$. A mass m is attached to the upper end of the rod, while the sliding sleeve constraint horizontally oscillates in time through the displacement $u_g(t)$.

rotation has to be evaluated outside the constraint. Neglecting the distributed inertia effects, the governing equation for $\theta(s,t)$ is provided by the elastica

$$B\,\theta''(s,t) + N_x(t)\,\cos\theta(s,t) - N_y(t)\,\sin\theta(s,t) = 0, \qquad s \in [L-\ell(t), L], \tag{3}$$

where the prime denotes differentiation with respect to s, $N_x(t)$ and $N_y(t)$ are the components along x and y axes of the internal action resultant $R(t)$, which is inclined at (the counter-clockwise) angle $\beta(t)$ with respect to the undeformed configuration,

$$N_x(t) = R(t)\sin\beta(t), \qquad N_y(t) = -R(t)\cos\beta(t). \tag{4}$$

The differential equation (3) is complemented by the boundary condition of null moment at the coordinate $s = L$ (neglecting the rotational inertia of the mass),

$$\theta'(L,t) = 0, \tag{5}$$

and the algebraic equation provided by the tangential force balance at the sliding sleeve exit involving the configurational force (Armanini et al., 2019)

$$N_y(t) = -\frac{\mathsf{M}^2(t)}{2B}, \tag{6}$$

where $\mathsf{M}(t)$ is the bending moment at the sliding sleeve entrance, $\mathsf{M}(t) = B\,\theta'(L-\ell(t),t)$, which is given by

$$\mathsf{M}(t) = N_x(t)\,y_L(t) - N_y(t)\,x_L(t), \tag{7}$$

while $x_L(t)$ and $y_L(t)$ are the relative coordinates of the attached mass,

$$x_L(t) = x(L,t), \qquad y_L(t) = y(L,t). \tag{8}$$

It is highlighted that Eq. (6) is the approximated version of the expression obtained in Armanini et al. (2019), by neglecting the possible contribution from the rotational inertia of the rod. The approximation presently introduced is motivated by the fact that the sliding velocity $\dot{\ell}(t)$ is much smaller than the longitudinal wave velocity in the rod.

The internal force components can be obtained through D'Alembert's principle as

$$N_x(t) = -m\left[\ddot{x}_L(t) + \ddot{u}_g(t)\right] - c(t)\left[\dot{x}_L(t) + \dot{u}_g(t)\right], \qquad N_y(t) = -m\left[\ddot{y}_L(t) + g\right] - c(t)\,\dot{y}_L(t), \tag{9}$$

where the overdot denotes differentiation with respect to the time t, and $c(t)$ is a linear time-variable viscosity coefficient defined as

$$c(t) = 2\,\zeta\,\sqrt{\frac{3\,m\,B}{\ell^3(t)}}, \tag{10}$$

introduced to model the dissipation of the rod and the air drag effects outside the sliding sleeve through the non-dimensional parameter $\zeta \geq 0$.

The spatial integration of the elastica (3) provides the end's relative coordinates $x_L(t)$ and $y_L(t)$ and the internal action components $N_x(t)$ and $N_y(t)$ as

$$\begin{aligned} x_L(t) &= \ell(t)\left\{\mathcal{A}_1(t)\sin\beta(t) - \mathcal{A}_2(t)\cos\beta(t)\right\}, \quad N_x(t) = \frac{B}{\ell^2(t)}\left[\mathcal{K}(k(t)) - \mathcal{K}(\sigma(t),k(t))\right]^2\sin\beta(t), \\ y_L(t) &= \ell(t)\left\{\mathcal{A}_1(t)\cos\beta(t) + \mathcal{A}_2(t)\sin\beta(t)\right\}, \quad N_y(t) = -\frac{B}{\ell^2(t)}\left[\mathcal{K}(k(t)) - \mathcal{K}(\sigma(t),k(t))\right]^2\cos\beta(t), \end{aligned} \tag{11}$$

where $\mathcal{K}(k(t))$ and $\mathcal{K}(\sigma(t),k(t))$ are the complete and incomplete elliptic integrals of the first kind, respectively,

$$\begin{aligned} k(t) &= \sin\left(\frac{\theta_L(t)-\beta(t)}{2}\right), \qquad \mathcal{A}_1(t) = -1 + \frac{2\left[\mathcal{E}(k(t)) - \mathcal{E}(\sigma(t),k(t))\right]}{\mathcal{K}(k(t)) - \mathcal{K}(\sigma(t),k(t))}, \\ \sigma(t) &= -\arcsin\left[\frac{1}{k(t)}\,\sin\frac{\beta(t)}{2}\right], \quad \mathcal{A}_2(t) = -\frac{2\,k(t)\,\cos\sigma(t)}{\mathcal{K}(k(t)) - \mathcal{K}(\sigma(t),k(t))}, \end{aligned} \tag{12}$$

with $\theta_L(t) = \theta(L,t)$, while $\mathcal{E}(k)$ and $\mathcal{E}(\sigma,k)$ are the complete and incomplete elliptic integrals of the second kind. Considering the results from the spatial integration (11), the configurational force balance (6) can be rewritten as

$$\cos\beta(t) = 2\left\{\left[2\left(\mathcal{E}(k(t)) - \mathcal{E}(\sigma(t),k(t))\right) - \left(\mathcal{K}(k(t)) - \mathcal{K}(\sigma(t),k(t))\right)\right]\sin\beta(t)\,\cos\beta(t) + k(t)\,\cos\sigma(t)\cos(2\beta(t))\right\}^2. \tag{13}$$

The dynamics of the structural system is therefore governed by a (DAE) differential–algebraic system of five equations composed by (i.) the two algebraic kinematic Eqs. $(11)_1$ and $(11)_3$, (ii.) the configurational force balance Eq. (13), and (iii.) the two following equations of motion

$$\begin{cases} m\left[\ddot{u}_g(t) + \ddot{x}_L(t)\right] + c(t)\left[\dot{u}_g(t) + \dot{x}_L(t)\right] - \frac{B}{\ell^2(t)}\left[\mathcal{K}(k(t)) - \mathcal{K}(\sigma(t),k(t))\right]^2\sin\beta(t) = 0, \\ m\left[g + \ddot{y}_L(t)\right] + c(t)\,\dot{y}_L(t) - \frac{B}{\ell^2(t)}\left[\mathcal{K}(k(t)) - \mathcal{K}(\sigma(t),k(t))\right]^2\cos\beta(t) = 0. \end{cases} \tag{14}$$

The dynamic response can be solved for the five unknowns in time, $x_L(t)$, $y_L(t)$, $\ell(t)$, $\theta_L(t)$ and $\beta(t)$, for the respective given initial conditions, fixed set of structural parameters m, B, L, g, ζ, and prescribed sliding sleeve motion $u_g(t)$.

3.2. Analytical periodic oscillation through asymptotic expansion

In order to obtain an analytical prediction for the dynamics of the structure subject to time-harmonic motion of the sliding sleeve (1), the differential system (14) governing the relative coordinates $x_L(t)$ and $y_L(t)$ of the end of the rod is approximated through its asymptotic expansion for small end rotation $\theta_L(t)$ under the assumption of null viscous dissipation ($\zeta = 0$) as

$$\begin{cases} m\,\ddot{x}_L(t) + \frac{3B}{\ell^3(t)}\,x_L(t) = m\,\omega^2\,\bar{u}_g\,\cos(\omega t), \\ m\left[g + \ddot{y}_L(t)\right] = \frac{\mathsf{M}^2(t)}{2B}, \end{cases} \tag{15}$$

where $\omega = 2\pi\bar{f}$ is the angular frequency. Under small rotation $\theta_L(t)$ and by assuming $\beta(t) \approx \pm\pi/2$ (corresponding to the condition $|N_y(t)| \ll |N_x(t)|$), the following second-order expansions hold

$$\mathsf{M}(t) = 2\,\frac{B\,\theta_L(t)}{\ell(t)}, \qquad x_L(t) = \frac{2}{3}\,\ell(t)\,\theta_L(t), \qquad y_L(t) = \ell(t)\left[1 - \frac{4}{15}\,\theta_L^2(t)\right]. \tag{16}$$

Introducing a reference rod's length $\ell_m \in (0, L)$, defined as a mean value measured during a given interval of time (to be specified later), a dimensionless time τ_m can be introduced as

$$\tau_m = t\sqrt{\frac{g}{\ell_m}}, \tag{17}$$

together with other dimensionless quantities, namely, the dimensionless load p_m, the dimensionless angular frequency Ω_m, the dimensionless oscillation amplitude U_m, the dimensionless external length $\lambda(\tau_m)$, and the attached mass dimensionless coordinates $\xi(\tau_m)$ and $\eta(\tau_m)$,

$$p_m = \frac{m\,g\,\ell_m^2}{B}, \quad \Omega_m = \omega\sqrt{\frac{\ell_m}{g}}, \quad U_m = \frac{\bar{u}_g}{\ell_m}, \quad \lambda(\tau_m) = \frac{\ell(t)}{\ell_m}, \quad \xi(\tau_m) = \frac{x_L(t)}{\ell_m}, \quad \eta(\tau_m) = \frac{y_L(t)}{\ell_m}, \tag{18}$$

so that the approximated equations of motion (15) can be rewritten in the following non-dimensional form

$$\begin{cases} \overset{**}{\xi}(\tau_m) + \frac{3}{p_m\,\lambda^3(\tau_m)}\,\xi(\tau_m) = \Omega_m^2\,U_m\,\cos(\Omega_m\,\tau_m), \\ 1 + \overset{**}{\eta}(\tau_m) - \frac{2\,\theta_L^2(\tau_m)}{p_m\,\lambda^2(\tau_m)} = 0, \end{cases} \tag{19}$$

where the superscript symbol $*$ stands for the derivative of the relevant quantity with respect to the dimensionless time τ_m. The end's rotation $\theta_L(\tau_m)$ and dimensionless external length $\lambda(\tau_m)$ are sought as the following periodic functions in the dimensionless time τ_m

$$\theta_L(\tau_m) = \varepsilon_\theta \cos(\Omega_m \tau_m), \qquad \lambda(\tau_m) = 1 - \varepsilon_\ell \cos(2\Omega_m \tau_m). \tag{20}$$

where ε_θ and ε_ℓ are the small dimensionless amplitudes of the rotation and of the external length oscillations. By assuming the periodic response (20), the dimensionless equations of motion (19) truncated at the smallest order reduce to

$$\begin{cases} 2\left[6\,\varepsilon_\theta - p_m\,\Omega_m^2(3\,U_m + 2\,\varepsilon_\theta)\right]\cos(\Omega_m\,\tau_m) - 3\,\varepsilon_\ell\left[2\,\varepsilon_\theta - p_m\,\Omega_m^2\,(3\,U_m + 8\,\varepsilon_\theta)\right]\cos(3\,\Omega_m\,\tau_m) \approx 0, \\ 15\left[p_m - \varepsilon_\theta^2 + \dfrac{p_m\,\varepsilon_\ell^2\,(1 - 8\,\Omega_m^2)}{2}\right] - \left[15\,\varepsilon_\theta^2 + 30\,p_m\,\varepsilon_\ell - p_m\,\Omega_m^2\left(8\,\varepsilon_\theta^2 + 60\,\varepsilon_\ell\right)\right]\cos(2\,\Omega_m\,\tau_m) \approx 0. \end{cases} \tag{21}$$

The annihilation of the time-independent term in Eq. $(21)_2$ leads to

$$p_m = \frac{\varepsilon_\theta^2}{1 - 4\,\varepsilon_\ell^2\,\Omega_m^2}, \qquad \text{or, equivalently,} \qquad \varepsilon_\theta = \pm\sqrt{p_m}\,\sqrt{1 - 4\,\varepsilon_\ell^2\,\Omega_m^2}, \tag{22}$$

the latter showing that two twin solutions exist, one with the rotation $\theta_L(\tau_m)$ in phase ($\varepsilon_\theta > 0$) and another in counter-phase ($\varepsilon_\theta < 0$) with the imposed motion $u_g(t)$ of the sliding sleeve.

Assuming that $\varepsilon_\ell\,\Omega_m \ll 1$, the last equation reduces to

$$p_m = \varepsilon_\theta^2, \qquad \text{or, equivalently,} \qquad \varepsilon_\theta = \pm\sqrt{p_m}, \tag{23}$$

which in turn simplify Eqs. (21) to

$$\begin{cases} 2\,\varepsilon_\theta\left[6 - \varepsilon_\theta\,\Omega_m^2(3\,U_m + 2\,\varepsilon_\theta)\right]\cos(\Omega_m\,\tau_m) - 3\,\varepsilon_\theta\,\varepsilon_\ell\left[2 - \varepsilon_\theta\,\Omega_m^2\,(3\,U_m + 8\,\varepsilon_\theta)\right]\cos(3\,\Omega_m\,\tau_m) \approx 0, \\ \varepsilon_\theta^2\left[15 + 30\,\varepsilon_\ell - \Omega_m^2\left(8\,\varepsilon_\theta^2 + 60\,\varepsilon_\ell\right)\right]\cos(2\,\Omega_m\,\tau_m) \approx 0. \end{cases} \tag{24}$$

The expansion (24) shows that equations of motion are satisfied at the smallest order when

$$\begin{cases} 6 - \varepsilon_\theta\,\Omega_m^2\left(3\,U_m + 2\,\varepsilon_\theta\right) \approx 0, \\ 15 - \Omega_m^2\left(8\,\varepsilon_\theta^2 + 60\,\varepsilon_\ell\right) \approx 0, \end{cases} \tag{25}$$

whose solution can be obtained under three specific regimes, differing in the inequality ruling the orders of ε_ℓ and ε_θ, namely:

$$|\varepsilon_\ell| \ll |\varepsilon_\theta|^2, \qquad |\varepsilon_\ell| \approx |\varepsilon_\theta|^2, \qquad \text{and} \qquad |\varepsilon_\ell| \gg |\varepsilon_\theta|^2.$$

Among the above three regimes, only the solution referred to the second one is presented below, because it was found to be the only one capable to predict the stable response obtained from the direct time integration of the differential–algebraic system $(11)_1$, $(11)_3$, (13), and (14) in the next Section. However, the solutions corresponding to the two remaining regimes are included for completeness in Appendix A.

Under the assumption $|\varepsilon_\ell| \approx |\varepsilon_\theta|^2$, the system (25) defines the following asymptotic order for the dimensionless amplitude U_m and angular frequency Ω_m

$$U_m \approx |\varepsilon_\theta|, \qquad \Omega_m \approx \frac{1}{|\varepsilon_\theta|}, \tag{26}$$

implying the validity of the following solutions for $p_m \to 0$ and for finite values of $p_m\,\Omega_m^2$,

$$U_m = \frac{2\left|3 - p_m\,\Omega_m^2\right|}{3\,p_m\,\Omega_m^2}\sqrt{p_m}, \qquad \varepsilon_\ell = \frac{15 - 8\,p_m\,\Omega_m^2}{60\,p_m\,\Omega_m^2}\,p_m. \tag{27}$$

A replacement in Eq. $(27)_1$ of the non-dimensional quantities U_m, p_m, and Ω_m with their dimensional counterparts (18) leads to the following twin equations

$$2\left(\frac{m\,\omega^2\,\ell_m^3}{B} - 3\right) \pm 3\,\bar{u}_g\,\ell_m\,\omega^2\sqrt{\frac{m}{g\,B}} = 0, \qquad \text{for} \qquad \ell_m \neq \ell_c = \sqrt[3]{\frac{3B}{m\,\omega^2}}, \tag{28}$$

where ℓ_c represents the length of the clamped rod (with an attached mass m and bending stiffness B) at resonance with the sliding sleeve motion frequency ω. By setting two dimensionless positive parameters σ and ρ, both unrestricted in their magnitude, as

$$\sigma = \frac{\bar{u}_g}{3\sqrt{g}}\sqrt[3]{\frac{3}{2}}\sqrt[6]{\frac{m\,\omega^8}{B}} = \frac{1}{3}\sqrt[3]{\frac{3}{2}}\,U_m\,\sqrt[6]{p_m}\,\sqrt[3]{\Omega_m^4} > 0, \qquad \rho = \ell_m\sqrt[3]{\frac{2}{3}}\sqrt[3]{\frac{m\,\omega^2}{B}} = \sqrt[3]{\frac{2}{3}}\sqrt[3]{p_m\,\Omega_m^2} > 0, \tag{29}$$

Eqs. (28) can be rewritten as the two following cubic dimensionless twin equations

$$\rho^3 - 2 \pm 3\,\rho\,\sigma = 0, \qquad \text{for } \rho \neq \sqrt[3]{2}, \tag{30}$$

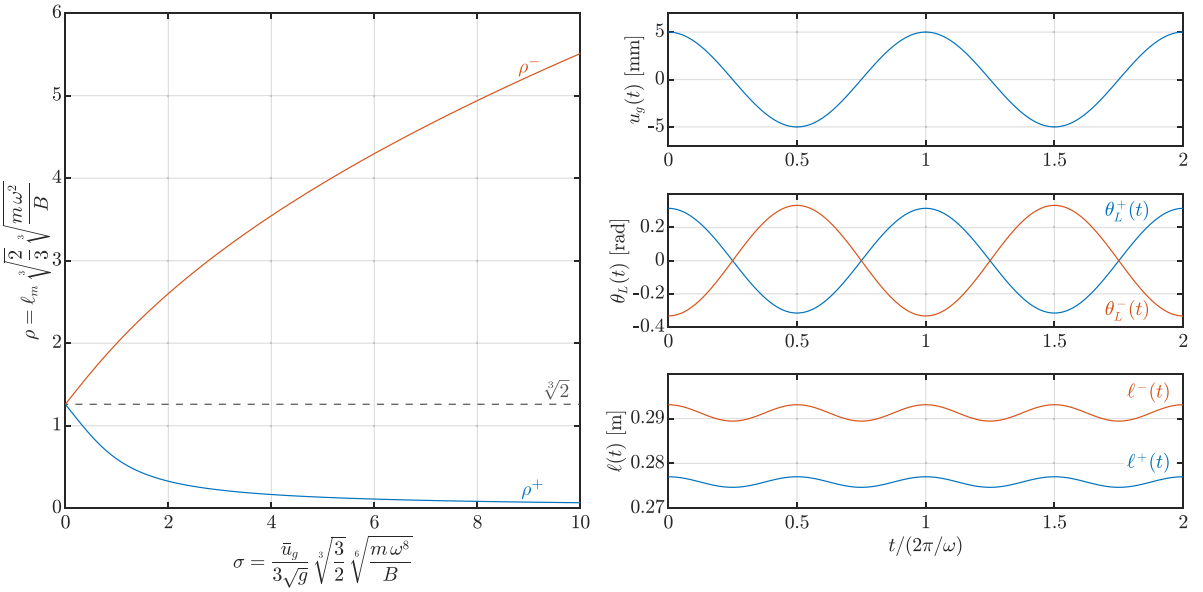

Fig. 6. (Left part) Twin solutions $\rho^{\pm}$ versus parameter σ (solid lines), Eq. (31). In the limit of vanishing σ, the two corresponding average lengths $\ell_m^{\pm}$ converge to the same value $\ell_c = \sqrt[3]{3B/(m\omega^2)}$ (provided by $\rho = \sqrt[3]{2}$, dashed line), defining the length of the clamped rod at resonance with the constraint motion frequency. (Right part) Time-series of (top) the sliding sleeve harmonic motion $u_g(t) = \bar{u}_g \cos(\omega t)$ and the twin periodic solutions in terms of (centre) the rotation $\theta_L^{\pm}(t) = \pm|\varepsilon_\theta| \cos(\omega t)$ and (bottom) the external length $\ell^{\pm}(t) = \ell_m^{\pm}[1 - \varepsilon_\ell \cos(2\omega t)]$ for parameters $m = 0.2$ kg, $B = 1.5$ Nm^2, $\omega = 10\pi$ rad/sec, and $\bar{u}_g = 0.005$ m. The input motion $u_g(t)$ and the output motion $\theta(t)$ can be in phase or in counter-phase, each one corresponding to a different value of average external length ℓ_m but to the same dimensionless amplitude ε_ℓ.

each one admitting a corresponding real and positive solution

$$\rho^{\pm}(\sigma) = \frac{\sqrt[3]{\left(1 + \sqrt{1 \pm \sigma^3}\right)^2} \mp \sigma}{\sqrt[3]{1 + \sqrt{1 \pm \sigma^3}}}, \tag{31}$$

and reported as functions of the dimensionless displacement amplitude σ at the sliding sleeve entrance in Fig. 6 (left). It is noted that in the limit case of vanishing values of σ the two solutions ρ^+ and ρ^- converge to the same value,

$$\lim_{\sigma \to 0} \rho^{\pm}(\sigma) = \sqrt[3]{2}, \tag{32}$$

and therefore both the two average lengths $\ell_m^{\pm}$ tend to converge to length ℓ_c of the clamped system at resonance,

$$\lim_{\frac{\bar{u}_g}{\sqrt{g}} \sqrt[6]{\frac{m\omega^8}{B}} \to 0} \ell_m^{\pm} = \ell_c. \tag{33}$$

The twin solutions $\theta_L^{\pm}(t) = \pm|\varepsilon_\theta| \cos(\omega t)$ and $\ell^{\pm}(t) = \ell_m^{\pm}[1 - \varepsilon_\ell \cos(2\omega t)]$ are shown in Fig. 6 (right) for the parameters $m = 0.2$ kg, $B = 1.5$ Nm^2, $\omega = 10\pi$ rad/sec, and $\bar{u}_g = 0.005$ m. Note that the rod's end rotation $\theta_L^+(t)$ is in phase with the sliding sleeve motion $u_g(t)$, while $\theta_L^-(t)$ is in counter-phase, and that, although the twin solutions appear to be far from each other in Fig. 6 on the left, the difference in dimensional terms is small for the case under consideration ($\ell_m^- \approx 1.056\ell_m^+$), as it can be appreciated from the graph of $\ell(t)$ (Fig. 6, right bottom part).

It is interesting to note that the present asymptotic analysis shows that the periodic motion is a solution for the dynamic response of the structure in the limit case of small rotations and high frequencies. Although based on these simplifying assumptions, it provides a very good prediction for the average length ℓ_m of the part of the rod external to the sliding sleeve, as shown through the comparison with the numerical simulations in Section 4 and with the experimental measurements in Section 5. Moreover, the present solution reveals the self-tuning property of the system, disclosing how the average length ℓ_m of the periodic motion changes with varying the oscillation amplitude $\bar{u}_g$ and angular frequency ω.

4. From periodic to quasi-periodic response

The asymptotic periodic solution presented in the previous section was derived with reference to the equations of motion approximated under the assumption of small values of ε_θ and ε_ℓ. As a result, the obtained analytical prediction is relevant when $|U_m| \sim 1/|\Omega_m| \to 0$, according to Eq. (26). Furthermore, the stability of such periodic response remains an open issue. In order

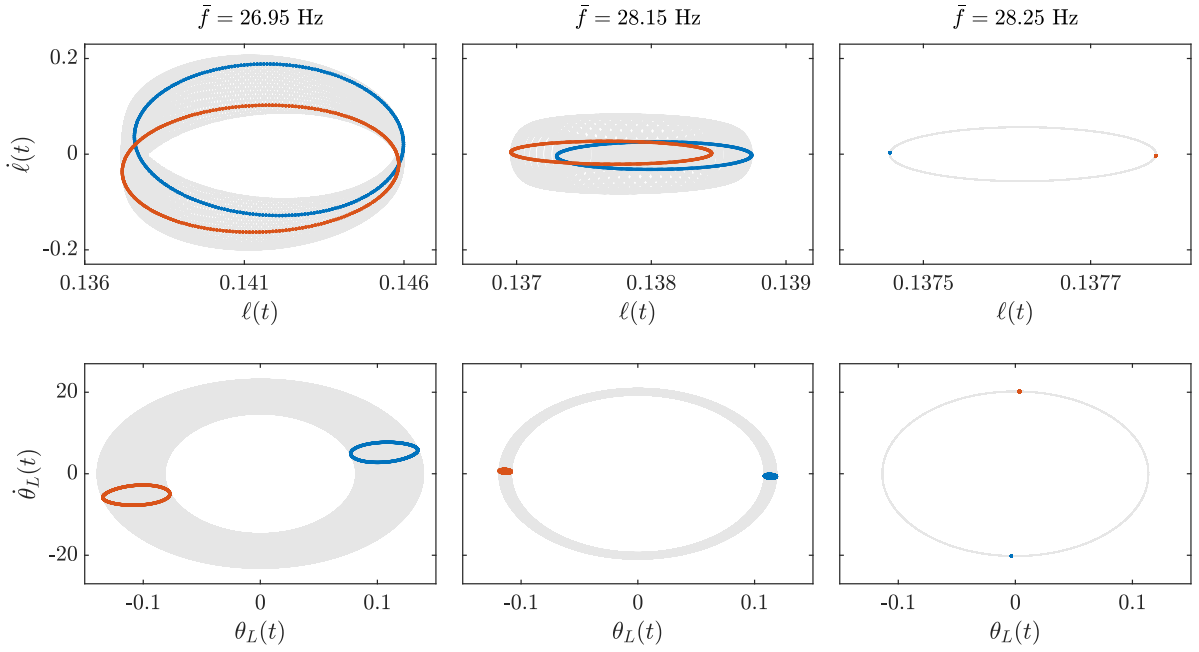

Fig. 7. Projections of the phase portraits and the Poincaré sections for the response of System A, calculated by direct numerical integration of the equations of motion, for two quarter-period shifted phases of $\ell(t)$ (upper part) and two half-period shifted phases of $\theta(t)$ (lower part). Two qualitatively different dynamic responses are shown: (i.) quasi-periodic motion for excitation frequency $\bar{f} = 26.95$ Hz (left) and $\bar{f} = 28.15$ Hz (centre) and (ii.) periodic motion for $\bar{f} = 28.25$ Hz (right), where the transition from the former to the latter occurs through a frequency decrease. The blue dots correspond to $t_1 = k/\bar{f}$ and the red dots to $t_2 = (k+1/2)/\bar{f}$ for the rotation $\theta_L(t)$ and to $t_2 = (k+1/4)/\bar{f}$ for the external length $\ell(t)$. The grey regions denote the extent of the phase space covered in time by the system.

to provide a more complete view on the mechanical response and to assess the stability of the sustained motion, the nonlinear equations of motion (14) are numerically integrated in time.

For the purposes of the numerical integration, the order of the differential equations (14) is reduced by producing pairs of first-order differential equations. Then, the ordinary differential–algebraic equation system consisting of Eqs. (11), (13), and the reduced-order version of Eqs. (14) are discretized in time and the Crank–Nicolson method, adapted to ODEs, is used to proceed from one timestep to the next. The final algorithm was programmed using MATLAB (source code available as Supplementary Material). The obtained numerical predictions for the system response reveal that the mass can display three different types of motion at varying input parameters: (i.) periodic; (ii.) quasi-periodic; and (iii.) divergent, the latter leading either to a complete injection ($\ell(t) \to 0$) or ejection ($\ell(t) > L$) of the rod. The periodic and quasi-periodic vibrations represent a sustained motion around a finite value for the rod's external length, where the interplay between the gravitational and configurational forces prevent the fall of the mass.

By considering $B = 1.4363$ Nm and $\bar{u}_g = 5$ mm, the two types of sustained motion are shown in Figs. 7 and 8 for System A (characterized by $m = 0.1$ g and $\zeta = 0.02$) and in Figs. 9 and 10 for System B (characterized by $m = 0.197$ g and $\zeta = 0.005$, with the former value representative of the experimental setup corresponding to $m_L = 130$ g, under the rod-lumped mass approximation, meaning that $m = m_L + \gamma L$). More specifically, the phase portraits of $\ell(t)$ and $\theta_L(t)$ are reported in Figs. 7 and 9 together with their Poincaré sections, while the respective Fast Fourier Transforms $P_{\theta_L}(f)$ and $P_{\ell}(f)$ are reported in Figs. 8 and 10. The results are reported when the transient effects due to the initial conditions on the motion are dissipated.

The Poincaré sections are shown for two shifted timings t_1 (blue dots) and t_2 (red dots), with $t_1 = k/\bar{f}$ and $t_2 = (k+1/2)/\bar{f}$ for the rotation $\theta_L(t)$ and with $t_1 = k/\bar{f}$ and $t_2 = (k+1/4)/\bar{f}$, for the external length $\ell(t)$, with $k \in \mathbb{N}$ defining the timings within the relevant interval. Moreover, the whole set of states occupied by the system is drawn as a grey region. The Poincaré sections appear as a single point (and the whole set of states as an ellipse) when the response is periodic ($\bar{f} = 28.25$ Hz in Fig. 7, $\bar{f} = 2.5$ Hz in Fig. 9) or as a set of points resembling a closed loop when the response is quasi-periodic ($\bar{f} = 26.95$ Hz and $\bar{f} = 28.15$ Hz in Fig. 7, $\bar{f} = 3.2$ Hz and $\bar{f} = 3.5$ Hz in Fig. 9). Therefore, it follows that the transition from periodic to quasi-periodic dynamics is shown in Figs. 7 and 8 (Figs. 9 and 10) may occur at decreasing (or at increasing) sliding sleeve oscillation frequency $\bar{f}$ for System A (System B).

The change from periodic to quasi-periodic can be also appreciated from the Fast Fourier Transforms shown in Figs. 8 and 10 through the appearance of additional peaks in correspondence to several frequencies different from $2\bar{f}$ for $P_{\ell}(f)$ and to $\bar{f}$ for $P_{\theta_L}(f)$.

The conditions providing the transition between the different types of motion and when the sustained motion cannot occur are displayed over a wider set of frequencies through the diagrams reported in Figs. 11 and 12 for Systems A and B, respectively. In these diagrams, the numerical values of the average length ℓ_m^{num} (solid black line) and the corresponding maximum $\ell_{\max}^{\text{num}}$ and minimum

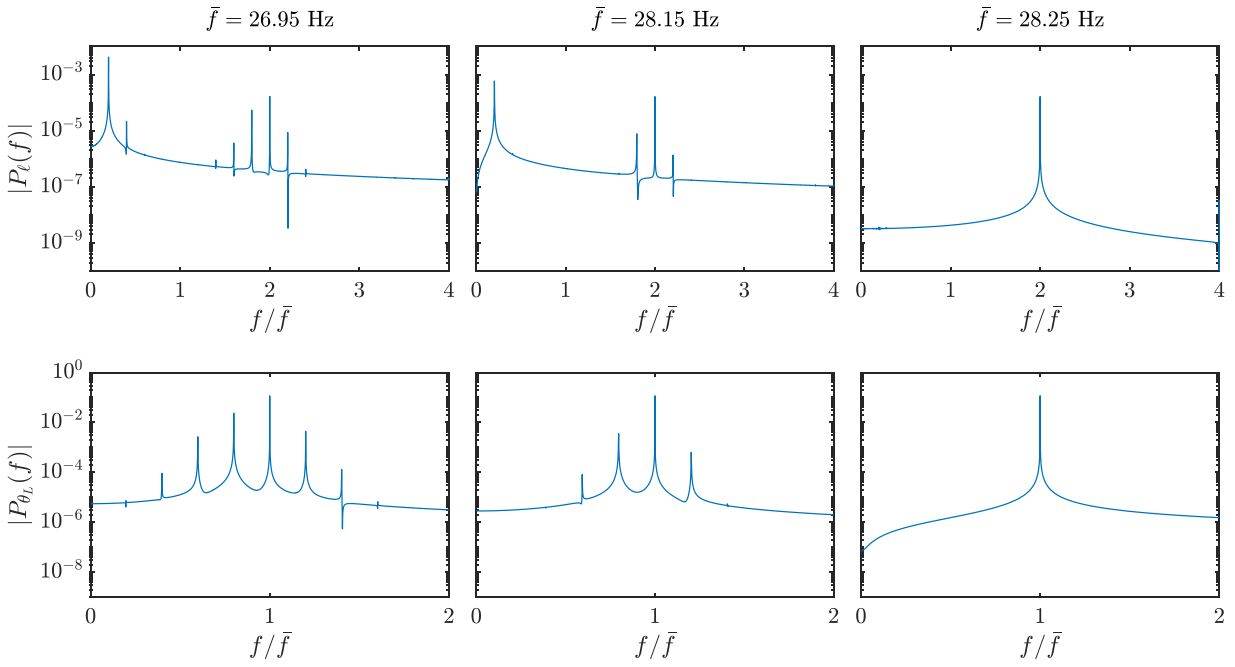

Fig. 8. As for Fig. 7, except that the spectrum of the response is analysed, as calculated using the Fast Fourier Transform. A single peak in the graphs occurring at rational values of $f/\bar{f}$ implies a periodic response, while peaks appearing for other values of $f/\bar{f}$ imply a quasi-periodic response.

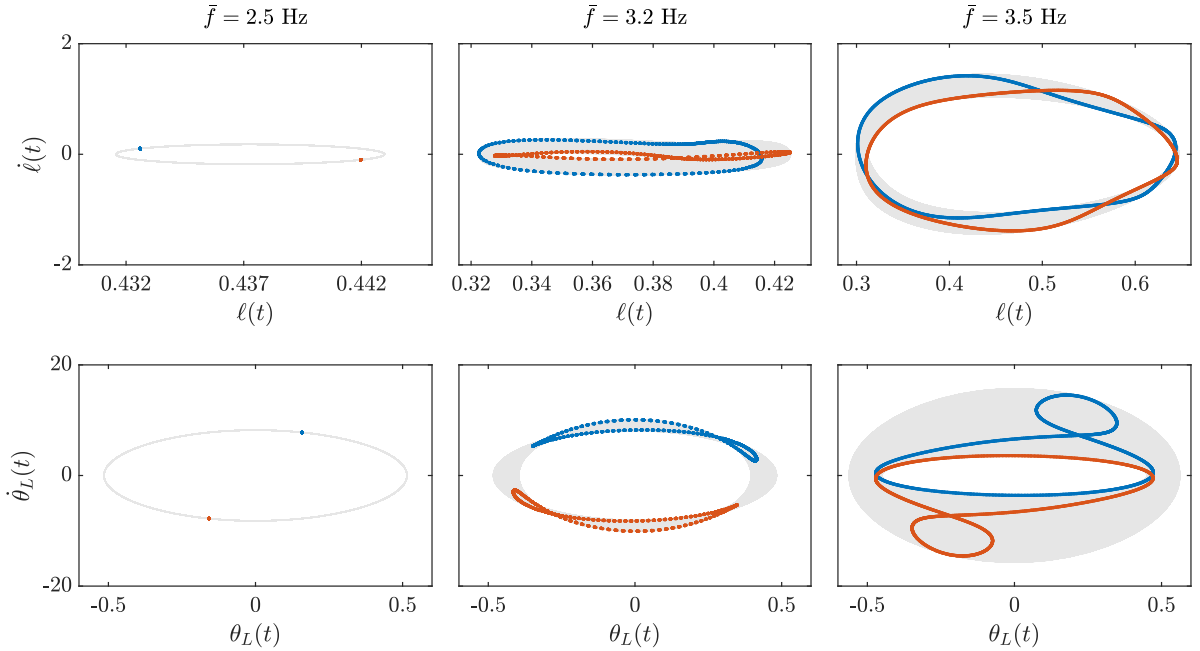

Fig. 9. As for Fig. 7, but for System B and showing that the transition from quasi-periodic ($\bar{f} = 3.5$ Hz, right, and $\bar{f} = 3.2$ Hz, centre) to periodic ($\bar{f} = 2.5$ Hz, left) response can occur through a frequency decrease.

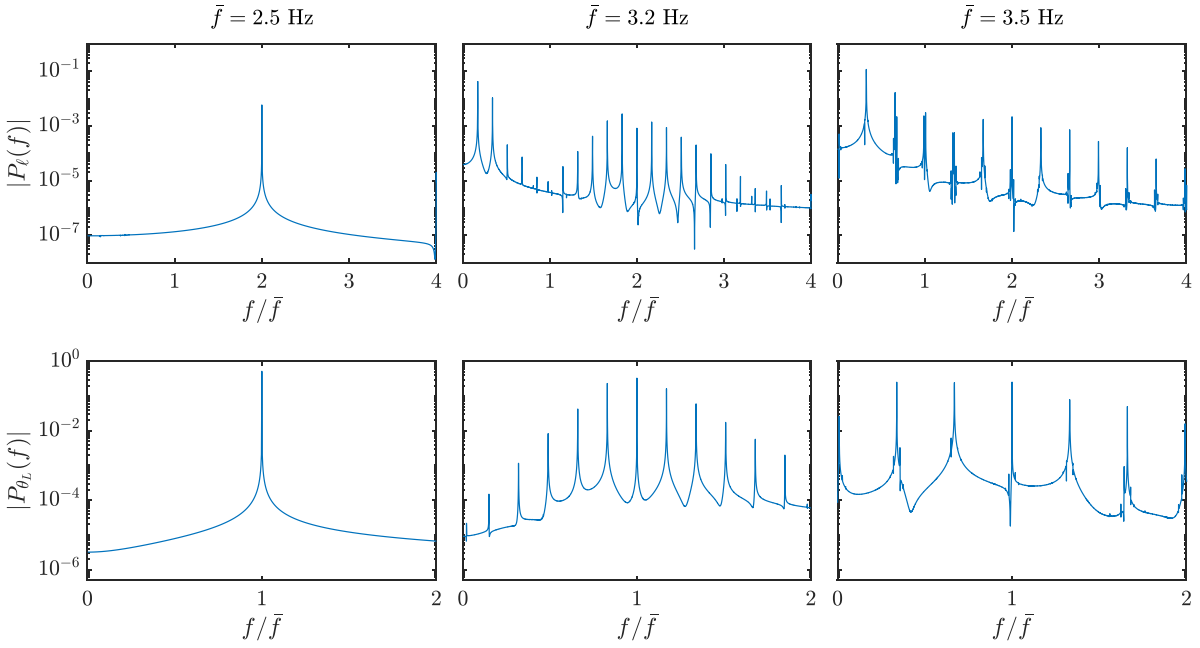

Fig. 10. As for Fig. 8, except that the spectrum refers to System B as considered in Fig. 9.

$\ell^{\text{num}}_{\text{min}}$ length values (dash-dotted black lines) are reported as functions of the frequency $\bar{f}$ and computed for each frequency value as

$$\ell^{\text{num}}_{m}\left(\bar{f}\right) = \frac{\bar{f}}{k}\int_{t_0}^{t_0+k/\bar{f}} \ell(t)\,\mathrm{d}t, \qquad \ell^{\text{num}}_{\text{max}}\left(\bar{f}\right) = \max_{t\in[t_0,t_0+k/\bar{f}]}\{\ell(t)\}, \qquad \ell^{\text{num}}_{\text{min}}\left(\bar{f}\right) = \min_{t\in[t_0,t_0+k/\bar{f}]}\{\ell(t)\}, \tag{34}$$

where t_0 is a time instant after the transient effects are dissipated and the integer k (assumed equal to 60) is the number of oscillation periods used to determine ℓ^{num}_{m}, $\ell^{\text{num}}_{\text{max}}$, and $\ell^{\text{num}}_{\text{min}}$. The two average lengths ℓ^{+}_{m} (blue) and ℓ^{-}_{m} (red), analytically estimated through Eq. (31), are also included in the diagrams, confirming how the asymptotic expression ℓ^{-}_{m} provides an excellent estimation for the self-tuned external length ℓ.

Interestingly, the diagram shows that the transition from periodicity (green region, marked with 'P') to quasi-periodicity (light green region, marked with 'QP') is the result of a *dynamic bifurcation* of the system, where both $\ell^{\text{num}}_{\text{min}}$ and $\ell^{\text{num}}_{\text{max}}$ display a visible discontinuity in their derivative. Such dynamic bifurcation is followed by a monotonic increase in the differences $\ell^{\text{num}}_{\text{max}} - \ell^{\text{num}}_{m}$ and $\ell^{\text{num}}_{m} - \ell^{\text{num}}_{\text{min}}$, eventually ending in the loss of quasi-periodicity due to the complete injection of the rod within the sliding sleeve (red region, marked with 'IN'). Under this circumstance, due to the nonlinearities inherent to the increasing oscillation amplitude of the rod's external length, the relation $|\varepsilon_\ell| \approx |\varepsilon_\theta|^2$ does not hold anymore and the periodic solution (20), obtained through an asymptotic technique, becomes no longer representative of the structural response at varying frequency of the sliding sleeve. Moreover, it is also worth to mention that the loss of sustained motion may theoretically occur even without passing through a quasi-periodic response, as shown at low frequencies ($\bar{f} \approx 1$ Hz) in Fig. 12. Overall, the diagrams show that the sustained motion occurs when $\bar{f} > 26.45$ Hz for System A and for 1.11 Hz $< \bar{f} <$ 3.60 Hz and $\bar{f} > 26.35$ Hz for System B. This result confirms that, in agreement with the experimental observations in Section 2 (Figs. 2–4), the present structural model does display not only a (stable) self-tuned sustained motion for high frequencies but it may also display it for an 'island' of intermediate set of frequencies depending on the elastic, inertial, and dissipation parameters. Note that, while the present model based on linear damping never displayed chaotic behaviour, the introduction (not pursued here) of nonlinear dissipation, for instance friction, may deeply change the dynamics of the system, thus leading to chaos.

5. Experimental setup and validation of the self-tuning external length value

The experimental setup developed for testing the sliding rod is shown in Fig. 13 and was designed, manufactured and tested at the Instabilities Laboratory of the University of Trento.

The sliding sleeve is realized through two parallel arrays of rollers kept at a small fixed distance by means of two acrylic panels. More specifically, the distance between the roller arrays is set to maintain the constrained part of the rod straight, but still free to slide. The sliding sleeve constraint device is connected through a stinger to an electromagnetic actuator (ElectroForce Linear motor 3300 Series II by Bose, frequency range 1–100 Hz, rated peak force SINE/RANDOM 3000N, max rated travel 25 mm) and screwed

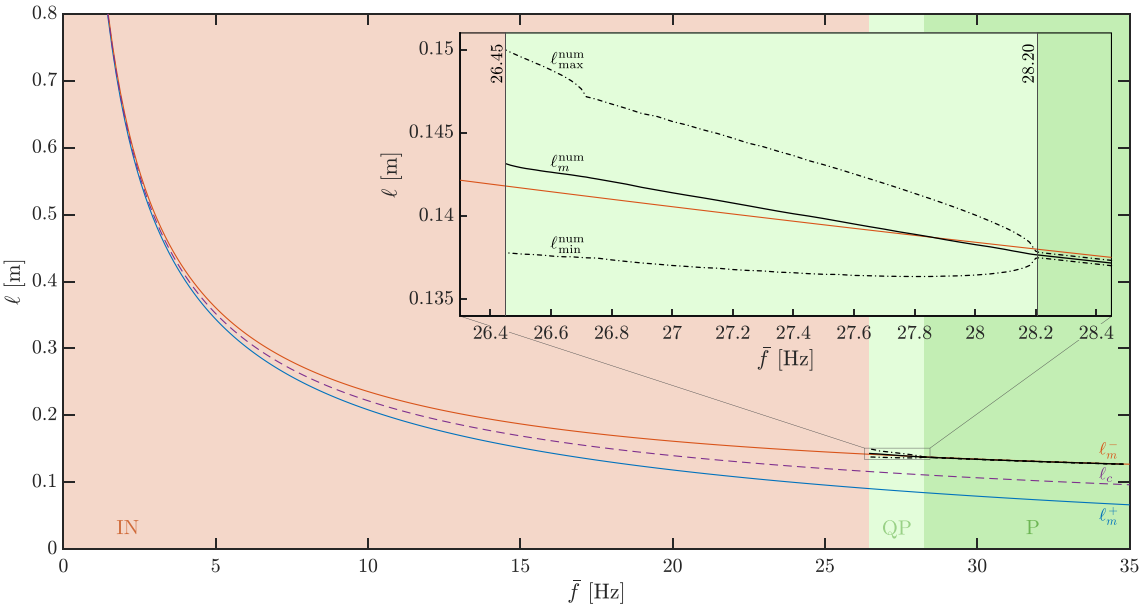

Fig. 11. Bifurcation diagram, showing the transition from periodic (green region, marked with 'P') to quasi-periodic (light green region, marked with 'QP') response of System A, when the excitation frequency is decreased to the value $\bar{f} \approx 28.20$ Hz. When the frequency $\bar{f}$ is further reduced to reach the frequency $\bar{f} \approx 26.45$ Hz, the rod suffers injection (red region, marked with 'IN'). The blue and red lines represent the two asymptotic evaluations for the average external lengths ℓ_m^+ and ℓ_m^-, respectively, while the length ℓ_c of the clamped rod at resonance is reported as a dashed purple line. The inset highlights the bifurcation and the transition points occurring at $\bar{f} = 28.20$ Hz and at $\bar{f} = 26.45$ Hz, respectively.

Table 1
Properties of the carbon-fibre rods used in the experiments.

Property	Value
Thickness	2.04 mm
Width	25.33 mm
Length L	800 mm
Bending stiffness B	1.4363 Nm^2
Mass (γL)	67 g

on a rail system that ensures motion along the horizontal direction only. Before each test, the sliding sleeve was oiled using Ballistol.

Carbon fibre rods are used in the experiments because of their modest material damping. The rods have a thin rectangular cross section and are realized by cutting a carbon-fibre sheet. The rod properties are summarized in Table 1. The lumped mass m_L is made with a pair of interchangeable metallic discs mounted at the rod's end. Two values of the lumped mass m_L were selected, 130 and 303 g. The equipment was designed to allow the excitation frequency $\bar{f}$ and amplitude $\bar{u}_g$ to lie within the ranges $[0, 20]$ Hz and $[0, 10]$ mm, respectively.

The rod's dynamics was recorded during the experiments with a Phantom High Speed V2640 camera and a Sony PXW-FS7 camera and the related videos were post-processed using a Matlab script in order to extract the time-histories of the relative coordinates, $x_L(t)$ and $y_L(t)$, of the mass and the external length of the rod $\ell(t)$.

Quantitative experimental results are reported in Fig. 14 for every pair of values $\bar{u}_g$ and m_L by performing the experiments of type (ii). In addition to the trajectories reported in Fig. 2, the experimental results are also shown in Fig. 14 in terms of period-averaged external length $\ell_a^{(k)}$ at the kth period of the sliding sleeve oscillation, evaluated as

$$\ell_a^{(k)} = \frac{1}{t_{k+1} - t_k} \int_{t_k}^{t_{k+1}} \ell(t)\, \mathrm{d}t, \qquad k \in \mathbb{N}, \tag{35}$$

where t_k (t_{k+1}) denotes the time instant at which the period begins (terminates).

The experimentally evaluated values of $\ell_a^{(k)}$ appear as a cloud of grey dots (included as data collection and visible as a real-time collection in the videos available as Supplementary Material), satisfactorily matching the asymptotically obtained average external lengths, ℓ_m^+ and ℓ_m^-, evaluated (for the undissipated system, $\zeta = 0$) through Eq. (31) by considering $m = m_L + \gamma L$. The average external lengths, ℓ_m^+ and ℓ_m^-, are obtained under the assumption $|\varepsilon_\ell| \approx |\varepsilon_\theta|^2$ and are complemented by reporting the length of the resonant clamped-free rod ℓ_c. It follows that a major result of the experimental campaign is the validation of the relation between the self-tuning external rod's length ℓ and the prescribed frequency of the sliding sleeve, $\bar{f}$, Fig. 14. In a rough sense, the external

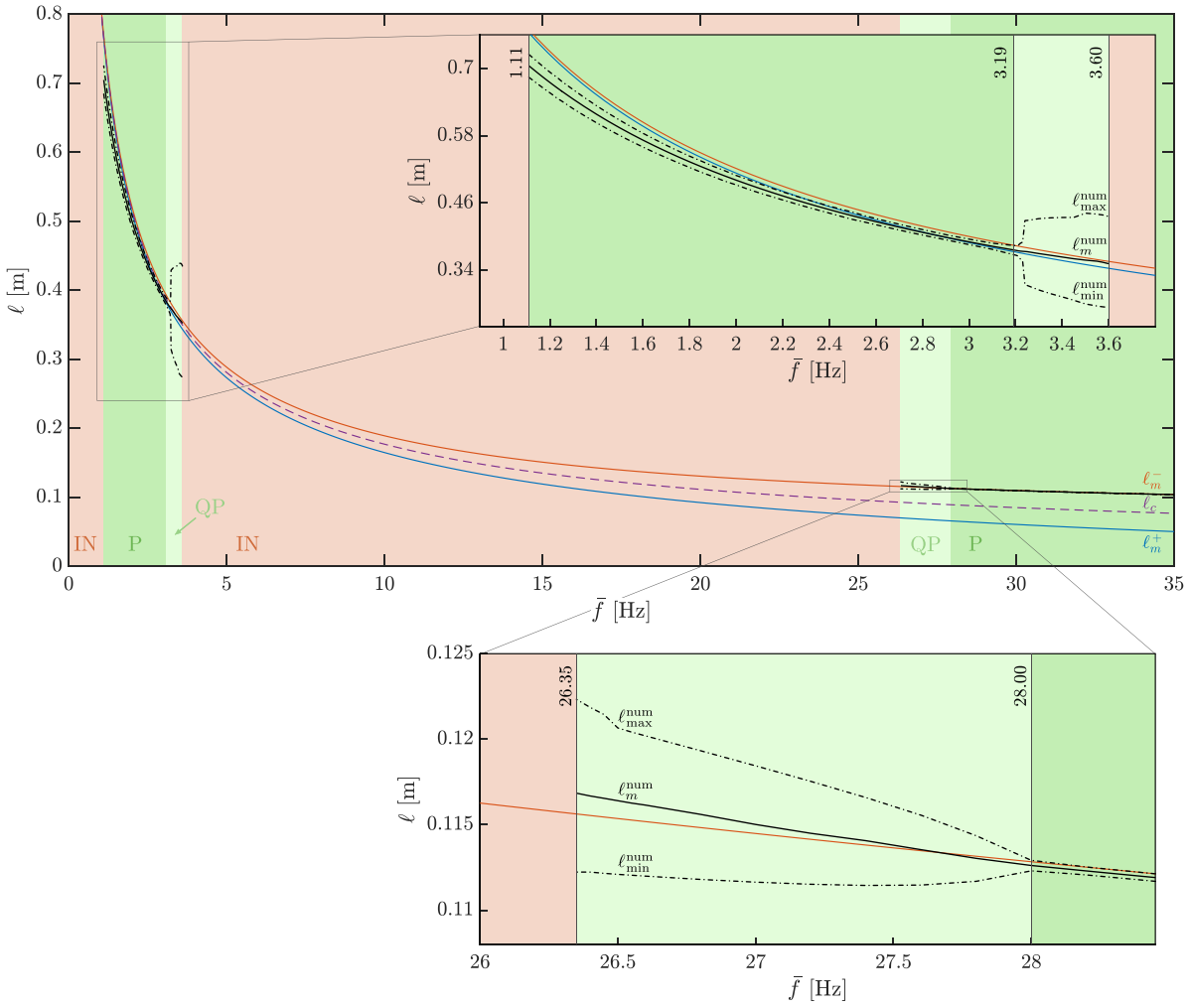

Fig. 12. As for Fig. 11, except that System B is analysed. Two ranges of frequencies are found (highlighted in the two insets) within which the rod is subject to sustained motion. The loss of sustained motion can occur without displaying an intermediate quasi-periodic dynamics.

length of the rod ℓ is shown to self-adjust (in an average sense) approximately within the range $[\ell^{+}_{m}, \ell^{-}_{m}]$, so that the rod mass system evolves to reach a configuration close to its resonant state and a sustained motion is realized. However, the sustained motion can be terminated by the occurrence of an instability in which the rod trajectory degenerates into a final injection.

6. Conclusions

A special kind of elastic inverted pendulum, for which static equilibrium is impossible at small deflections, has been analysed. Interestingly, its inverted configuration can be maintained against gravity when a transverse vibration is applied at the lower constraint. For specific ranges of system parameters the structure is shown (analytically, numerically, and experimentally) to self-tune its external length and display a sustained motion, obtained through an interplay between the downward (constant) gravity force and the upward (time-varying) configurational force, the latter strictly related to the elasticity of the structure.

For the analysed structure, the two following main features are found.

- Existence of twin asymptotic periodic motions, around two different finite values of the average rod's length ℓ^{+}_{m} and ℓ^{-}_{m}, external to the sliding sleeve. These two values are shown to be close to ℓ_c, corresponding to the length of a clamped rod at resonance at the input frequency. Accurate numerical simulations, accounting for a full nonlinear behaviour, have shown that only one (ℓ^{-}_{m}) among the two periodic solutions may be stable.
- Stability of the sustained motion occurs only within a certain range of frequencies and amplitudes. Here, the sliding rod displays self-tuning properties by spontaneously adjusting its length as a result of the change in the oscillation amplitude and frequency.

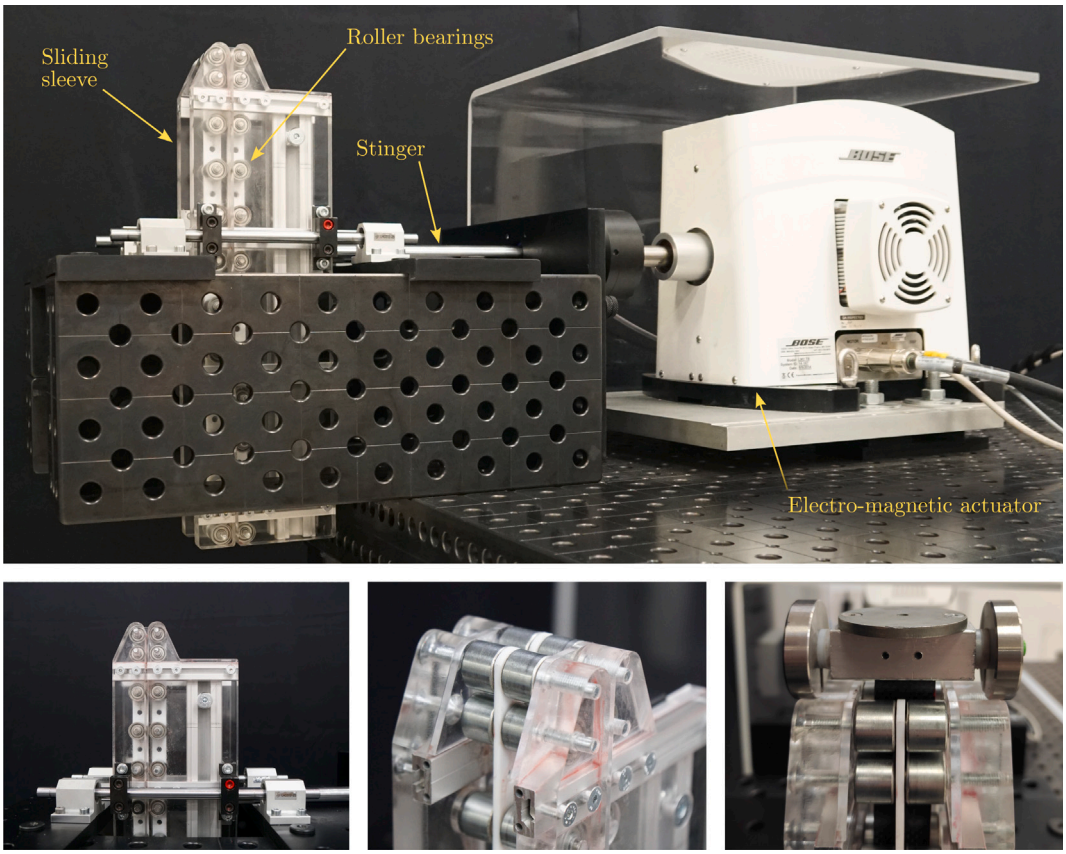

Fig. 13. Experimental setup designed for the oscillating sliding-sleeve system (realized at the Instabilities Lab of the University of Trento). Upper part: general arrangement. Lower part: details of the sliding sleeve (left and centre) and of the lumped mass m_L (right).

The presented results may find application in compliant systems, including resonant metamaterials, where the self-tuning capability via configurational constraints can be exploited for the development of wave mitigation devices and environmental energy harvesters based on flexible mechanisms. Moreover, the introduced mechanical concept can drive novel control applications where a longitudinal output can be tuned through a transverse input, with the purpose of chasing designed trajectories or to reach targeted positions.

CRediT authorship contribution statement

P. Koutsogiannakis: Formal analysis, Investigation, Methodology, Experimental tests and data analysis, Software, Validation, Visualization, Writing – original draft, Writing – review & editing. **D. Misseroni:** Methodology, Experimental tests, Supervision, Writing – review & editing. **D. Bigoni:** Formal analysis, Methodology, Supervision, Writing – review & editing, Funding acquisition. **F. Dal Corso:** Conceptualization, Project administration, Formal analysis, Methodology, Supervision, Writing – original draft, Writing – review & editing, Funding acquisition.

Declaration of competing interest

The authors declare that they have no known competing financial interests or personal relationships that could have appeared to influence the work reported in this paper.

Data availability

Videos and data collection from experiments and source code for numerical integration are available as Supplementary material.

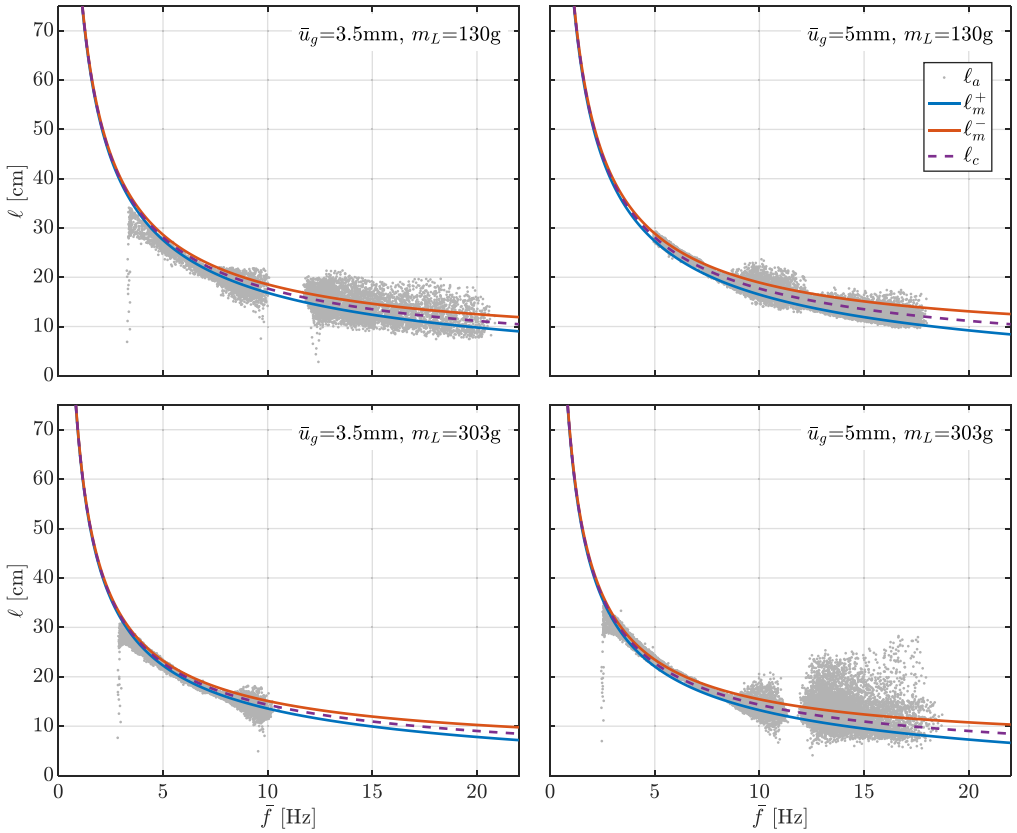

Fig. 14. External length ℓ of the rod versus oscillation frequency $\bar{f}$ for systems with lumped mass $m_L = \{130, 303\}$ g and constraint amplitude $\bar{u}_g = \{3.5, 5\}$ mm. The grey points correspond to the period-averaged external length $\ell_a^{(k)}$ evaluated from the experimental measurements through Eq. (35) (data collection available as Supplementary Material). The blue and red solid lines respectively correspond to the asymptotic predictions ℓ_m^+ and ℓ_m^-, Eq. (31). while the dashed purple line represents the length ℓ_c of the clamped rod at resonance. Absence of stability for the sustained motion can be observed for an intermediate range of frequencies where a gap is observed between the grey dots (the absence of grey dots at higher frequencies is due to the lack of experimental data), resulting in a complete injection of the rod. When the sustained motion is stable, the system displays self-tuning property through its spontaneous adjustment in the value of the external length ℓ as a consequence of a small variation in the oscillation frequency $\bar{f}$.

Acknowledgements

PK gratefully acknowledges the financial support from the European Union's Horizon 2020 research and innovation programme under the Marie Sklodowska-Curie grant agreement 'INSPIRE - Innovative ground interface concepts for structure protection' PITN-GA-2019-813424-INSPIRE. DM, DB, and FDC acknowledge financial support from the European Research Council (ERC) under the European Union's Horizon 2020 research and innovation programme (Grant agreement No. ERC-ADG-2021-101052956-BEYOND).

Appendix A. Asymptotic solution under regimes for which $|\varepsilon_\ell| \approx |\varepsilon_\theta|^2$

The asymptotic solutions corresponding to the regimes $|\varepsilon_\ell| \ll |\varepsilon_\theta|^2$ and $|\varepsilon_\ell| \gg |\varepsilon_\theta|^2$ are reported.

A.1. Regime $|\varepsilon_\ell| \gg |\varepsilon_\theta|^2$

In this regime the dimensionless amplitude U_m and frequency Ω_m have the following asymptotic order

$$|U_m| \gg |\varepsilon_\theta|, \qquad |\Omega_m| \approx \frac{1}{\sqrt{|\varepsilon_\ell|}}, \tag{36}$$

implying the following relations at $p_m \to 0$ and for finite values of $\sqrt{p_m}\,\Omega_m^2$

$$U_m = \pm\frac{2}{\sqrt{p_m}\Omega_m^2}, \qquad \varepsilon_\ell = \frac{1}{4\sqrt{p_m}\Omega_m^2}\sqrt{p_m}, \tag{37}$$

the latter showing that the solution defines $\varepsilon_\ell \approx \varepsilon_\theta$. Eq. (37) leads to the expressions for the average length ℓ_m and its normalized amplitude ε_ℓ as

$$\ell_m = \pm\frac{2}{\omega^2 \bar{u}_g}\sqrt{\frac{B}{m}}, \qquad \varepsilon_\ell = \pm\frac{\bar{u}_g}{8}\sqrt{\frac{mg}{B}}, \tag{38}$$

defining a gravity-insensitive average length ℓ_m.

A.2. Regime $|\varepsilon_\ell| \ll |\varepsilon_\theta|^2$

While in this regime the value ε_ℓ remains undefined, the dimensionless amplitude U_m and frequency Ω_m have the following asymptotic order

$$|U_m| \approx |\varepsilon_\theta|, \qquad |\Omega_m| \approx \frac{1}{|\varepsilon_\theta|}, \tag{39}$$

implying that the solutions valid at $p_m \to 0$ and for finite values of $p_m\,\Omega_m^2$ define

$$U_m = \pm\frac{2\sqrt{p_m}}{5}, \qquad \Omega_m = \frac{1}{2}\sqrt{\frac{15}{2p_m}}, \tag{40}$$

which can be rewritten in terms of the average length ℓ_m and the oscillation amplitude $\bar{u}_g$ as

$$\ell_m = \frac{1}{2}\sqrt[3]{\frac{15B}{m\omega^2}}, \qquad \bar{u}_g = \frac{1}{2}\sqrt[3]{\frac{9}{5\omega^4}}\sqrt[6]{\frac{B}{m}}\sqrt{g}. \tag{41}$$

Appendix B. Supplementary data

Supplementary material related to this article can be found online at https://doi.org/10.1016/j.jmps.2023.105452.

References

Alfalahi, H., Renda, F., Stefanini, C., 2020. Concentric tube robots for minimally invasive surgery: Current applications and future opportunities. IEEE Trans. Med. Robot. Bionics 2 (3), 410–424.

Armanini, C., Dal Corso, F., Misseroni, D., Bigoni, D., 2019. Configurational forces and nonlinear structural dynamics. J. Mech. Phys. Solids 130, 82–100.

Ballarini, R., Royer-Carfagni, G., 2016. A Newtonian interpretation of configurational forces on dislocations and cracks. J. Mech. Phys. Solids 95, 602–620.

Bigoni, D., Dal Corso, F., Bosi, F., Misseroni, D., 2015. Eshelby-like forces acting on elastic structures: theoretical and experimental proof. Mech. Mater. 80, 368–374.

Bigoni, D., Dal Corso, F., Misseroni, D., Bosi, F., 2014. Torsional locomotion. Proc. R. Soc. A 470 (2171), 20140599.

Eshelby, J.D., 1999. Energy relations and the energy-momentum tensor in continuum mechanics. In: Fundamental Contributions To the Continuum Theory of Evolving Phase Interfaces in Solids. Springer, pp. 82–119.

Gibus, D., Morel, A., Gasnier, P., Ameye, A., Badel, A., 2022. High performance piezoelectric vibration energy harvesting by electrical resonant frequency tuning. Smart Mater. Struct. 31 (12), 125012.

Hanna, J.A., Singh, H., Virga, E.G., 2018. Partial constraint singularities in elastic rods. J. Elasticity 133 (1), 105–118.

Kapitza, P.L., 1951. Dynamic stability of a pendulum when its point of suspension vibrates. Zh. Eksper. Teoret. Fiz. 21 (5), 588–597.

Lee, H., Lee, J.K., Seung, H.M., Kim, Y.Y., 2018. Mass-stiffness substructuring of an elastic metasurface for full transmission beam steering. J. Mech. Phys. Solids 112, 577–593.

Liakou, A., 2018a. Application of optimal control method in buckling analysis of constrained elastica problems. Int. J. Solids Struct. 141, 158–172.

Liakou, A., 2018b. Constrained buckling of spatial elastica: Application of optimal control method. J. Appl. Mech. 85 (8).

Liu, Y., Su, X., Sun, C.T., 2015. Broadband elastic metamaterial with single negativity by mimicking lattice systems. J. Mech. Phys. Solids 74, 158–174.

Ma, K.J., Tan, T., Liu, F.R., Zhao, L.C., Liao, W.H., Zhang, W.M., 2020. Acoustic energy harvesting enhanced by locally resonant metamaterials. Smart Mater. Struct. 29 (7), 075025.

Matlack, K.H., Bauhofer, A., Krödel, S., Palermo, A., Daraio, C, 2016. Composite 3D-printed metastructures for low-frequency and broadband vibration absorption. Proc. Natl. Acad. Sci. 113 (30), 8386–8390.

O'Reilly, O.M., 2015. Some perspectives on eshelby-like forces in the elastica arm scale. Proc. R. Soc. A 471 (2174), 20140785.

O'Reilly, O.M., 2017. Modeling Nonlinear Problems in the Mechanics of Strings and Rods. Springer.

Renda, F., Messer, C., Rucker, C., Boyer, F., 2021. A sliding-rod variable-strain model for concentric tube robots. IEEE Robot. Autom. Lett. 6 (2), 3451–3458.

Sipos, A.A., Várkonyi, P.L., 2020. The longest soft robotic arm. Int. J. Non-Linear Mech. 119, 103354.

Wang, L., Bertoldi, K., 2012. Mechanically tunable phononic band gaps in three-dimensional periodic elastomeric structures. Int. J. Solids Struct. 49 (19–20), 2881–2885.

Wang, Z.Q., Detournay, E., 2022. Eshelbian force on a steadily moving liquid blister. Internat. J. Engrg. Sci. 170, 103591.

Yu, L., Tang, L., Yang, T., 2020. Piezoelectric passive self-tuning energy harvester based on a beam-slider structure. J. Sound Vib. 489, 115689.